

A Chimera domain decomposition method with weak Dirichlet-Robin coupling for finite element simulation of particulate flows

Raphael Münster, Otto Mierka, Dmitri Kuzmin*, Stefan Turek

*Institute of Applied Mathematics (LS III), TU Dortmund University
Vogelpothsweg 87, D-44227 Dortmund, Germany*

Abstract

We introduce a new multimesh finite element method for direct numerical simulation of incompressible particulate flows. The proposed approach falls into the category of overlapping domain decomposition / Chimera / overset grid meshes. In addition to calculating the velocity and pressure of the fictitious fluid on a fixed background mesh, we solve the incompressible Navier-Stokes equations on body-fitted submeshes that are attached to moving particles. The submesh velocity and pressure are used to calculate the hydrodynamic forces and torques acting on the particles. The coupling with the background velocity and pressure is enforced via (i) Robin-type boundary conditions for an Arbitrary-Lagrangian-Eulerian (ALE) formulation of the submesh problems and (ii) a Dirichlet-type distributed interior penalty term in the weak form of the background mesh problem. The implementation of the weak Dirichlet-Robin coupling is discussed in the context of discrete projection methods and finite element discretizations. Detailed numerical studies are performed for standard test problems involving fixed and moving immersed objects. A comparison of Chimera results with those produced by fictitious boundary methods illustrates significant gains in the accuracy of drag and lift approximations.

Keywords: particulate flows, fictitious domains, embedded boundaries, finite element methods, overlapping grids, Chimera domain decomposition, Dirichlet–Robin coupling

1. Introduction

Numerical methods for direct numerical simulation (DNS) of incompressible flows around moving rigid particles can be classified into fixed mesh and deforming mesh approaches [5]. Prominent representatives of the latter family include immersed boundary methods [10, 15, 22] and fictitious domain formulations in which the rigid body motion inside the particles is enforced using distributed

*Corresponding author

Email address: {raphael.muenster,otto.mierka,dmitri.kuzmin,stefan.turek}@math.tu-dortmund.de (Raphael Münster, Otto Mierka, Dmitri Kuzmin*, Stefan Turek)

Lagrange multipliers (DLM, [3, 4, 14]), fictitious (surrogate, shifted, unfitted) boundary methods [11, 24, 25, 26, 27], subspace projections [1, 16], and other non-DLM alternatives [23, 18]. The resolving power of such approaches can be greatly improved by using mesh deformation techniques [1, 13, 28] or overlapping domain decomposition with moving submeshes [2, 6, 7, 8, 9]. The coupling conditions in the overlap region can again be enforced in different ways. Houzeaux and Codina [8] propose a Chimera method with Dirichlet/Neumann(Robin) coupling such that Dirichlet-type conditions are strongly enforced at nodal points inside and around immersed objects. The multimesh finite element method developed by Dokken et al. [2] achieves the coupling effect by incorporating suitable stabilization terms into the discontinuous Galerkin (DG) weak forms of interacting subproblems.

A common disadvantage of all fixed-mesh algorithms that constrain the velocity of a fictitious fluid at discrete locations is the lack of continuous dependence on the data. Indeed, a small displacement of a particle can activate or deactivate the Dirichlet constraint. Moreover, the volume of the constrained region changes abruptly leading to nonphysical temporal oscillations in the pressure field and, as a consequence, in forces acting on the particles. In the present paper, we cure this deficiency of Chimera-type domain decomposition methods by using a distributed interior penalty term instead of strongly imposed nodal constraints. The weak form of our background mesh problem differs from the unfitted finite element method presented in [2] in the structure of employed stabilization terms and in the way in which they are incorporated into the discrete projection method for the Navier–Stokes system. Our algorithm is simpler than the DG method from [2] and requires fewer degrees of freedom because we are using a continuous approximation to the velocity field. The results of our numerical experiments show that our modification of the Chimera method from [8] is robust and capable of delivering accurate DNS results at a fraction of the cost that a fixed-mesh fictitious boundary method would require.

The rest of this paper is organized as follows. A fictitious domain formulation of the particulate flow problem that we consider is presented in Section 2. The Chimera domain decomposition method introduced in Section 3 leads to a system of weakly coupled Navier-Stokes problems. In Section 4, we incorporate Dirichlet constraints into the weak form of the background mesh problem using the distributed interior penalty approach. In Section 5, we show how we update the velocity and pressure using the framework of discrete projection methods. The new Chimera penalty method for solving the coupled problem is summarized in Section 6 and compared with a modification in which the Dirichlet constraints are imposed strongly (as in the original method [8]). The numerical behavior of both versions is studied in Section 7, and some conclusions are drawn in Section 8.

2. Fictitious domain formulation

Let $\Omega \subset \mathbb{R}^d$, $d \in \{2, 3\}$ be a fixed fictitious domain. In our particulate flow model, Ω is filled with an incompressible Newtonian fluid that carries a suspension of N_p rigid particles (balls)

$$B_k(t) = \{\mathbf{x} \in \mathbb{R}^d : |\mathbf{x} - \mathbf{X}_k(t)| < R_k\}.$$

We subdivide Ω into $\Omega_p(t) := \bigcup_{k=1}^{N_p} B_k(t)$ and the subdomain $\Omega_f(t) := \Omega \setminus \bar{\Omega}_p(t)$ occupied by the fluid.

The evolution of the fluid-particle mixture is governed by the system [13, 26]

$$\rho_f \left(\frac{\partial \mathbf{u}}{\partial t} + \mathbf{u} \cdot \nabla \mathbf{u} \right) = -\nabla p + \nabla \cdot (2\mu_f \mathbf{D}(\mathbf{u})) \quad \text{in } \Omega_f(t), \quad (1a)$$

$$\nabla \cdot \mathbf{u} = 0 \quad \text{in } \Omega, \quad (1b)$$

$$\mathbf{u} = \mathbf{U} \quad \text{on } \bar{\Omega}_p(t) \quad (1c)$$

of generalized incompressible Navier–Stokes equations. Here \mathbf{u} is the velocity of the fluid, \mathbf{U} is the velocity of rigid body motion inside the particles, p is the pressure, and

$$\mathbf{D}(\mathbf{u}) = \frac{1}{2}(\nabla \mathbf{u} + \nabla \mathbf{u}^\top)$$

is the deformation rate tensor. The constant density and dynamic viscosity of the fluid phase are denoted by ρ_f and μ_f , respectively. For $\mathbf{x} \in \bar{B}_k(t)$, the velocity of the fictitious fluid is given by

$$\mathbf{U}(\mathbf{x}, t) = \mathbf{U}_k(t) + \boldsymbol{\omega}_k(t) \times (\mathbf{x} - \mathbf{X}_k), \quad (2)$$

where \mathbf{U}_k is the translational velocity and $\boldsymbol{\omega}_k$ is the angular velocity of the k th particle. The density, volume, and moment of inertia tensor of this particle are denoted by ρ_k , V_k , and \mathbb{I}_k , respectively.

For simplicity, we assume that the particles do not collide with each other or with solid walls. Therefore, we do not include repulsive or lubrication forces in the Newton–Euler equations

$$\rho_p V_k \frac{d\mathbf{U}_k}{dt} = \mathbf{F}_k + (\rho_p - \rho_f) V_k \mathbf{g}, \quad (3a)$$

$$\mathbb{I}_k \frac{d\boldsymbol{\omega}_k}{dt} = \mathbf{T}_k - \boldsymbol{\omega}_k \times (\mathbb{I}_k \boldsymbol{\omega}_k), \quad (3b)$$

where \mathbf{g} is the gravitational acceleration. The hydrodynamic force \mathbf{F}_k and torque \mathbf{T}_k are defined by

$$\mathbf{F}_k = - \int_{\partial B_k} \boldsymbol{\sigma} \mathbf{n} ds, \quad (4a)$$

$$\mathbf{T}_k = - \int_{\partial B_k} (\mathbf{x} - \mathbf{X}_k) \times (\boldsymbol{\sigma} \mathbf{n}) ds. \quad (4b)$$

Here \mathbf{n} denotes the unit outward normal and $\boldsymbol{\sigma} = -p\mathbf{I} + 2\mu_f \mathbf{D}(\mathbf{u})$, where \mathbf{I} is the identity tensor.

The problem statement is completed by imposing appropriate initial and boundary conditions. By default, we prescribe a given velocity profile at the inlet, the zero-stress condition at the outlet, and the no-slip condition on solid walls. The rigid body motion constraint (1c) defines both the no-slip Dirichlet boundary data for $\partial\Omega_p(t)$ and the velocity of the fictitious fluid contained in $\Omega_p(t)$.

3. Chimera domain decomposition

In our multimesh numerical method for solving the coupled problems (1) and (3), we calculate \mathbf{F}_k and \mathbf{T}_k using finite element approximations to \mathbf{u} and p on the body-fitted subdomains

$$\hat{\Omega}_k(t) = \{\mathbf{x} \in \mathbb{R}^d : R_k < |\mathbf{x} - \mathbf{X}_k(t)| < R_k + H_k\},$$

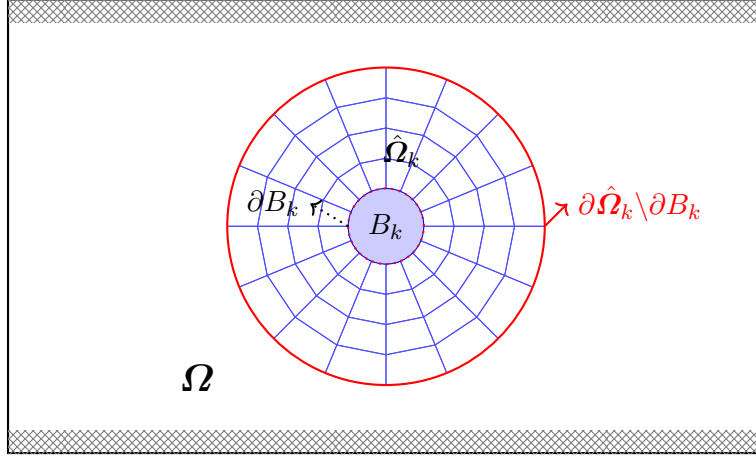


Figure 1: Subdomains of the Chimera domain decomposition method.

which are embedded into Ω as shown in Fig. 1. In this work, we assume that $\hat{\Omega}_k(t) \cap B_j(t) = \emptyset$ for $k \neq j$. The general case of overlapping domains is considered in [2, 9].

If the particle $B_k(t)$ were a planet, the associated subdomain $\hat{\Omega}_k(t)$ could be interpreted as the atmosphere of that planet. We denote the atmospheric velocity and pressure fields by $\hat{\mathbf{u}}$ and \hat{p} , respectively. The parameter $H_k > 0$ determines the width of the atmospheric layer around $B_k(t)$.

Following Houzeaux and Codina [8], we perform *iteration by subdomains* using coupling conditions of Dirichlet–Robin type. That is, the background fields \mathbf{u} and p influence the solution of

$$\rho_f \left(\frac{\partial \hat{\mathbf{u}}}{\partial t} + \hat{\mathbf{u}} \cdot \nabla \hat{\mathbf{u}} \right) = -\nabla \hat{p} + \nabla \cdot (2\mu_f \mathbf{D}(\hat{\mathbf{u}})) \quad \text{in } \hat{\Omega}_k(t), \quad (5a)$$

$$\nabla \cdot \hat{\mathbf{u}} = 0 \quad \text{in } \hat{\Omega}_k(t), \quad (5b)$$

$$\hat{\mathbf{u}} = \mathbf{U} \quad \text{on } \partial B_k(t), \quad (5c)$$

$$\hat{\boldsymbol{\sigma}} \mathbf{n} - \alpha(\hat{\mathbf{u}} \cdot \mathbf{n})\hat{\mathbf{u}} = \boldsymbol{\sigma} \mathbf{n} - \alpha(\mathbf{u} \cdot \mathbf{n})\mathbf{u} \quad \text{on } \partial \hat{\Omega}_k(t) \setminus \partial B_k(t) \quad (5d)$$

by providing the data of the Robin/Neumann boundary condition (5d), where $\alpha \geq 0$ is an interior penalty parameter and $\hat{\boldsymbol{\sigma}} = -\hat{p}\mathbf{I} + 2\mu_f \mathbf{D}(\hat{\mathbf{u}})$ is the total stress. The consistency relation

$$\mathbf{u} = \hat{\mathbf{u}} \quad \text{on } \bar{\hat{\Omega}}_k(t) \quad (6)$$

is satisfied by exact solutions to (1) and (5). Hence, it is appropriate to constrain a numerical approximation to the background velocity \mathbf{u} using a strong or weak form of the Dirichlet condition (6).

4. Finite element discretization

We discretize the velocity and pressure fields in space using the inf-sup stable $\mathbb{Q}_2\text{-}\mathbb{P}_1^{\text{disc}}$ finite element pair. The atmospheric subproblems (5) are solved on body-fitted meshes using an Arbitrary-

Lagrangian-Eulerian (ALE) formulation in the reference frame moving with the constant mesh velocity $\mathbf{w}_k(\mathbf{x}, t) = \mathbf{U}_k(t)$. Details of such moving mesh finite element (FE) methods can be found elsewhere [1, 12, 28] and are not discussed here. The ALE-FE approximation to $(\hat{\mathbf{u}}, \hat{p})$ is denoted by $(\hat{\mathbf{u}}_h, \hat{p}_h)$.

The fictitious domain problem (1) is solved using a fixed background mesh \mathcal{T}_h that consists of quadrilaterals (in 2D) or hexahedra (in 3D). Instead of enforcing the Dirichlet-type velocity constraints (1c) and (6) strongly at discrete locations (as in [8, 16, 25]), we incorporate them into a weak form of problem (1) using (a discrete counterpart of) the distributed interior penalty term

$$s(\hat{\mathbf{u}}, \mathbf{U}; \mathbf{u}, \mathbf{v}) = \gamma_{\max} \sum_{k=1}^{N_p} \left[\int_{\hat{\Omega}_k(t)} \beta_k(\mathbf{u} - \hat{\mathbf{u}}) \cdot \mathbf{v} d\mathbf{x} + \int_{B_k(t)} (\mathbf{u} - \mathbf{U}) \cdot \mathbf{v} d\mathbf{x} \right] \quad (7)$$

that depends on a penalty parameter $\gamma_{\max} \gg 1$ and a damping function $\beta_k : \hat{\Omega}_k \times \mathbb{R}_0^+ \rightarrow [0, 1]$ such as¹

$$\beta_k(\mathbf{x}, t) = \min \left(1, \max \left(0, \frac{R_k + 0.75H_k - |\mathbf{x} - \mathbf{X}_k(t)|}{0.25H_k} \right) \right).$$

The velocity \mathbf{U} of rigid body motion is defined by (2). In the discrete version of (7), integration is performed over the regions $\hat{\Omega}_{k,h}$ and $B_{k,h}$ that are covered by / enclosed by the ALE submesh.

Let \mathbf{V}_h and Q_h denote the finite element spaces for the velocity and pressure approximations on $\bar{\Omega}$, respectively. We seek $\mathbf{u}_h \in \mathbf{V}_h$ and $p_h \in Q_h$ such that

$$\begin{aligned} \int_{\Omega} \rho_f \left(\frac{\partial \mathbf{u}_h}{\partial t} + \mathbf{u}_h \cdot \nabla \mathbf{u}_h \right) \cdot \mathbf{v}_h d\mathbf{x} + \frac{\mu_f}{2} \int_{\Omega} \mathbf{D}(\mathbf{u}_h) : \mathbf{D}(\mathbf{v}_h) d\mathbf{x} + s_h(\hat{\mathbf{u}}_h, \mathbf{U}_h; \mathbf{u}_h, \mathbf{v}_h) \\ - \int_{\Omega} p_h \nabla \cdot \mathbf{v}_h d\mathbf{x} = 0, \quad \mathbf{v}_h \in \mathbf{V}_h, \end{aligned} \quad (8a)$$

$$\int_{\Omega} q_h \nabla \cdot \mathbf{u}_h d\mathbf{x} = 0, \quad \mathbf{q}_h \in Q_h. \quad (8b)$$

Figure 2 shows a snapshot of the region in which the ALE mesh attached to $B_k(t)$ intersects the fixed background mesh. The former provides the Dirichlet data $\hat{\mathbf{u}}_h$ for calculating $s_h(\hat{\mathbf{u}}_h, \mathbf{U}_h; \mathbf{u}_h, \mathbf{v}_h)$ defined by (7). The latter provides the Robin boundary data $\boldsymbol{\sigma}_h \mathbf{n} - \alpha(\mathbf{u}_h \cdot \mathbf{n})\mathbf{u}_h$ for updating $\hat{\mathbf{u}}_h$. The hydrodynamic force \mathbf{F}_k and torque \mathbf{T}_k are calculated using $\hat{\boldsymbol{\sigma}}_h = -\hat{p}_h \mathbf{I} + 2\mu_f \mathbf{D}(\hat{\mathbf{u}}_h)$ to approximate $\boldsymbol{\sigma}$ in (4). The high accuracy of the submesh approximation to the traction $\hat{\boldsymbol{\sigma}}_h \mathbf{n}$ on ∂B_k is a key advantage of the Chimera approach compared to one-mesh fictitious domain methods [16, 23, 25].

Remark 1. A remarkable property of the weak form (8) is that the interior penalty term (7) is well defined even for overlapping ‘atmospheres’ $\hat{\Omega}_k(t)$ and $\hat{\Omega}_j(t)$ of non-overlapping particles $B_k(t)$ and $B_j(t)$. The use of strongly imposed Dirichlet coupling conditions at background mesh nodes belonging

¹The nonnegative function β_k determines the strength of velocity penalization. It should vanish in a neighborhood of the interface $\Gamma_k(t) = \partial \hat{\Omega}_k(t) \setminus \partial B_k(t)$ to avoid interference with the Robin boundary condition (5d).

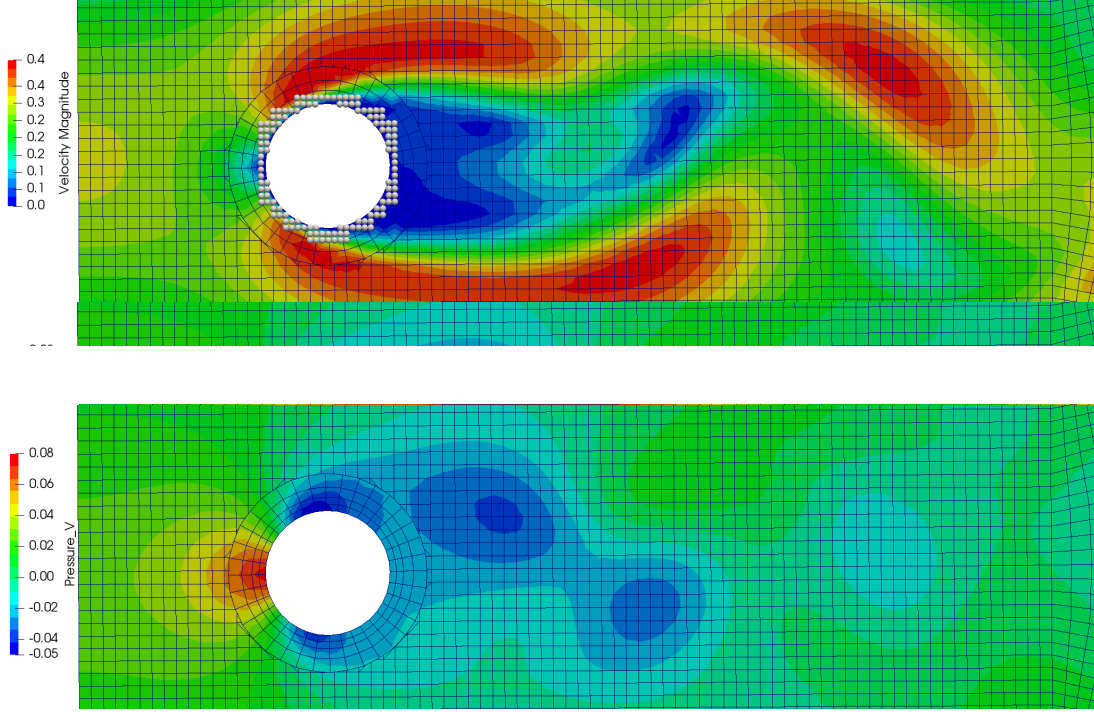


Figure 2: Chimera-type domain decomposition for a flow around a cylinder configuration. Velocity (top) and pressure (bottom) distribution on a uniform background mesh and an overlapping body-fitted submesh.

to the overlap region $\hat{\Omega}_k(t) \cap \hat{\Omega}_j(t)$ would require artificial averaging of submesh data. The proposed approach performs such averaging automatically by using penalty parameters depending on β_k and β_j . An extension to the case $\hat{\Omega}_k(t) \cap B_j(t) \neq \emptyset$ is feasible but would require adding a Dirichlet penalty term to the submesh problem for $\hat{\Omega}_k(t)$. Such extensions can be carried out following [2, 9].

5. Fractional-step method

Let $t^n = n\Delta t$, where Δt is a constant time step and $n \in \mathbb{N}_0$. Approximate solutions at the time level t^n will be referred to using the superscript n . At the beginning of each time step, we use the old submesh approximation $(\hat{\mathbf{u}}_h^n, \hat{p}_h^n)$ to calculate the surface integrals (4). The old background mesh approximation (\mathbf{u}_h^n, p_h^n) is used to calculate the data of the Robin boundary condition (5d). Then we update the positions of the particles and solve the discrete saddle point problems associated with ALE submeshes for $\hat{\Omega}_k(t)$. These problems are small and can be solved efficiently, e.g., using the local Multilevel Pressure Schur Complement (MPSC) method [19, 20, 21]. The updated approximation $(\hat{\mathbf{u}}_h^{n+1}, \hat{p}_h^{n+1})$ can then be substituted into the interior penalty term of problem (8) for $(\mathbf{u}_h^{n+1}, p_h^{n+1})$.

Using the two-level θ -scheme to discretize (8a) in time, we obtain a nonlinear system of the form

$$\begin{bmatrix} A(u^{n+1}) + D^{n+1} & B \\ B^T & 0 \end{bmatrix} \begin{bmatrix} u^{n+1} \\ p^{n+1} \end{bmatrix} = \begin{bmatrix} f^n + g^{n+1} \\ 0 \end{bmatrix}. \quad (9)$$

The contribution of the interior penalty term (7) is represented by $D^{n+1}u^{n+1} - g^{n+1}$, where D^{n+1} is a symmetric positive semi-definite matrix. In Appendix A below, we explicitly define all matrices and vectors that appear in (9), as well as the lumped approximation M_L to the consistent mass matrix M_C of the finite element space \mathbf{V}_h . Below we use M_L for preconditioning purposes.

We solve the discrete problem (9) approximately using the following fractional-step algorithm:

1. Solve the viscous Burgers system

$$[A(\tilde{u}^{n+1}) + D^{n+1}]\tilde{u}^{n+1} = f^n + g^{n+1} - Bp^n. \quad (10)$$

2. Solve the pressure Poisson system

$$B^T M_L^{-1} B(p^{n+1} - p^n) = \frac{1}{\Delta t} B^T \tilde{u}^{n+1}. \quad (11)$$

3. Correct the intermediate velocity

$$[M_L + \Delta t D^{n+1}]u^{n+1} = [M_L + \Delta t D^{n+1}]\tilde{u}^{n+1} - \Delta t B(p^{n+1} - p^n). \quad (12)$$

Note that we penalize the velocity not only in the Burgers step but also in the final update. The nonlinear system (10) is linearized about u^n or solved using a fixed-point iteration method [19].

Remark 2. Rearranging (12) and invoking (11), we find that the corrected velocity u^{n+1} satisfies

$$B^T u^{n+1} = \Delta t B^T M_L^{-1} D^{n+1}(\tilde{u}^{n+1} - u^{n+1}).$$

Hence, u^{n+1} is approximately divergence-free. Moreover, the residual of the constraint $B^T u^{n+1} = 0$ can be made as small as desired by performing additional outer iterations (cf. [19, 20]), in which the right-hand side of (10) is recalculated using the latest approximation to p^{n+1} instead of p^n .

6. Strong vs. weak Dirichlet coupling

For comparison purposes, we implemented a Chimera multimesh method in which the Dirichlet constraints are imposed strongly at *hole nodes* in $\hat{B}_k(t)$ and *fringe nodes* in $\hat{\Omega}_k$. The terminology that we use here is adopted from [8]. A node \mathbf{x}_i of a mesh cell crossed by $\partial B_k(t)$ is treated as a hole node if $\mathbf{x}_i \in B_k(t)$ and as a fringe node if $\mathbf{x}_i \in \hat{\Omega}_k(t)$. Following Houzeaux and Codina [8], we prescribe the fictitious boundary conditions $\mathbf{u}_h(\mathbf{x}_i) = \mathbf{U}(\mathbf{x}_i)$ and $\mathbf{u}_h(\mathbf{x}_i) = \hat{\mathbf{u}}_h(\mathbf{x}_i)$ at hole and fringe nodes, respectively. Details can be found in [8]. For a better comparison of Chimera methods with weak and strong Dirichlet coupling, the main algorithmic steps are summarized below for both versions.

The strong-form implementation will be referred to as *Chimera-S*. It represents a combination of the methods developed in [8] and [25, 26, 27]. The numerical solutions are updated as follows:

1. Solve the background mesh problem (1) using fictitious Dirichlet boundary conditions at hole nodes in the first outer iteration and at hole+fringe nodes in subsequent updates.
2. Solve the submesh problems (5) using interpolated background velocity \mathbf{u}_h and pressure p_h in the surface integral associated with the Robin boundary condition (5d).
3. Calculate \mathbf{F}_k and \mathbb{I}_k for each particle using the submesh stress $\hat{\boldsymbol{\sigma}}_h$ in the surface integrals (4).
4. Solve the discrete version of the Newton–Euler equations (3). Use the updated velocity \mathbf{U}_k and angular velocity $\boldsymbol{\omega}_k$ to determine the new position and orientation of particles.
5. Find the hole/fringe nodes corresponding to the updated position of particles, interpolate the submesh velocity $\hat{\mathbf{u}}_h$ to these nodes of the background mesh and go to Step 1 or exit.

At least two outer iterations need to be performed in this fictitious boundary Chimera method.

The implementation labeled *Chimera-W* incorporates the interior penalty term (7) into the discretized momentum equation (8a). The proposed algorithm consists of the following steps:

1. Calculate \mathbf{F}_k and \mathbb{I}_k for each particle using the submesh stress $\hat{\boldsymbol{\sigma}}_h$ in the surface integrals (4).
2. Solve the discrete version of the Newton–Euler equations (3). Use the updated velocity \mathbf{U}_k and angular velocity $\boldsymbol{\omega}_k$ to determine the new position and orientation of particles.
3. Solve the submesh problems (5) using interpolated background velocity \mathbf{u}_h and pressure p_h in the surface integral associated with the Robin boundary condition (5d).
4. Go to Step 1 if stronger coupling is desired.
5. Solve the background mesh problem (1) using the updated submesh velocity $\hat{\mathbf{u}}_h$ in the interior penalty term $s_h(\hat{\mathbf{u}}_h, \mathbf{U}; \mathbf{u}_h, \mathbf{v}_h)$ of the discretized momentum equation (8a).
6. Go to Step 1 if stronger coupling is desired.

In contrast to the Chimera-S version, this algorithm may be terminated after one outer iteration.

7. Numerical examples

In this section, we perform numerical studies of the Chimera-S and Chimera-W domain decomposition methods presented in Section 6. For comparison purposes, we also ran simulations using the classical fictitious boundary method [25, 26], in which no submeshes are used, and the background mesh is uniform. In this version (FBM), the constraint of rigid body motion (2) is enforced strongly at the hole nodes inside the particles. Since we are interested in applications to particulate flows, some of our investigations are focused on the accuracy of approximations to drag and lift forces. The unfitted treatment of embedded boundaries in the FBM approach results in large errors on coarse meshes. Moreover, hydrodynamic forces typically exhibit oscillatory behavior. The objective of our experiments is to show that the use of body-fitted submeshes leads to significant improvements.

7.1 DFG benchmark 2D-2

One of the most popular test problems in computational fluid dynamics (CFD) is known as the DFG benchmark 2D-2 [17]. It is designed to evaluate numerical algorithms for solving the incompressible Navier-Stokes equations under laminar flow conditions. Specifically, this benchmark provides reference data and computational setup for simulating the two-dimensional flow around a circular cylinder at the Reynolds number $Re=100$. The experimentally observed flow pattern exhibits periodic vortex shedding, known as the von Kármán vortex street. For an in-depth description of the benchmark, we refer the reader to [17]. The most important quantities and parameters are defined below.

The computational domain is a two-dimensional rectangular channel with a circular obstacle representing a cross section of a cylinder. The length and height of the channel are 2.2 units and 0.41 units, respectively. The cylinder has a diameter of 0.1 units and is centered at $(0.2, 0.2)$.

Assuming that the laminar flow is fully developed at the inlet, the parabolic velocity profile

$$\mathbf{u}(0, y) = \left(\frac{4Uy(0.41 - y)}{0.41^2}, 0 \right)$$

is prescribed on the inflow boundary ($x = 0$). The maximum velocity U is attained at $y = 0.205$.

The drag force F_d and the lift force F_l exerted by the fluid on the cylinder are given by

$$\begin{pmatrix} F_d \\ F_l \end{pmatrix} = \frac{1}{\rho_f} \int_{\partial B} \hat{\boldsymbol{\sigma}}_h \mathbf{n} ds,$$

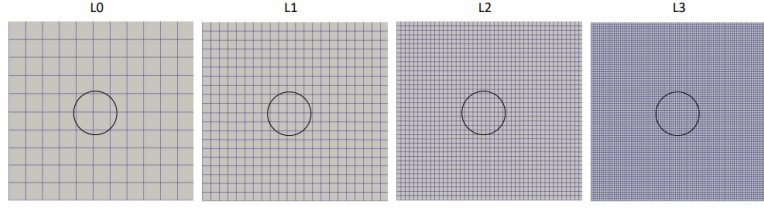
where $\hat{\boldsymbol{\sigma}}_h$ is the submesh approximation to $\boldsymbol{\sigma} = -p\mathbf{I} + 2\mu_f\mathbf{D}(\mathbf{u})$, and \mathbf{n} is the unit outward normal to the boundary ∂B of the cylinder. Using F_d and F_l , we compute the drag and lift coefficients

$$C_d = \frac{2F_d}{U_{\text{mean}}^2 L}, \quad C_l = \frac{2F_l}{U_{\text{mean}}^2 L}, \quad (13)$$

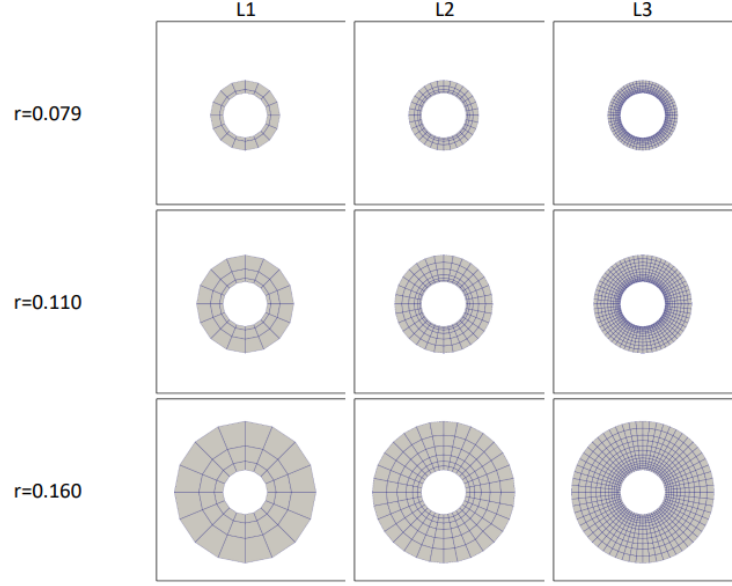
where $U_{\text{mean}} = 1.0$ is the average velocity at the inlet and $L = 0.1$ is the characteristic length. Because of periodic vortex shedding, the coefficients C_d and C_l vary over time.

We performed simulations for the DFG Benchmark 2D-2 using the FBM and Chimera-S methods. To leverage the advantages of using body-fitted submeshes and gain insights regarding appropriate choices of background mesh/submesh resolutions for our Chimera domain decomposition algorithms, we varied these resolutions and the outer radius of the submesh as shown in Fig. 3.

The evolution history of the drag and lift coefficients obtained with FBM and Chimera-S is presented in Figure 4-6. We have marked in the plots the reference values of C_d^{\min} , C_d^{\max} , C_d^{mean} , C_l^{\min} , C_l^{\max} and C_l^{mean} , as well as the evolution zone that is defined in previous publications of our research group [17, 21]. The legend for the cases under investigation is as follows: L1_110L2 corresponds to background mesh resolution L1, submesh radius $r = 0.110$, and submesh resolution L2. From the simulation results, we clearly see that all of these three parameters have an influence on the accuracy of the computation. The Chimera method achieves smoother force evolution than FBM and yields more accurate approximations, demonstrating its potential for improved efficiency and reliability.



(a) Benchmark mesh with an immersed cylinder on different levels of resolution.



(b) Body-fitted submeshes on different levels of resolution.

Figure 3: Background mesh and submeshes for the DFG Benchmark 2D-2.

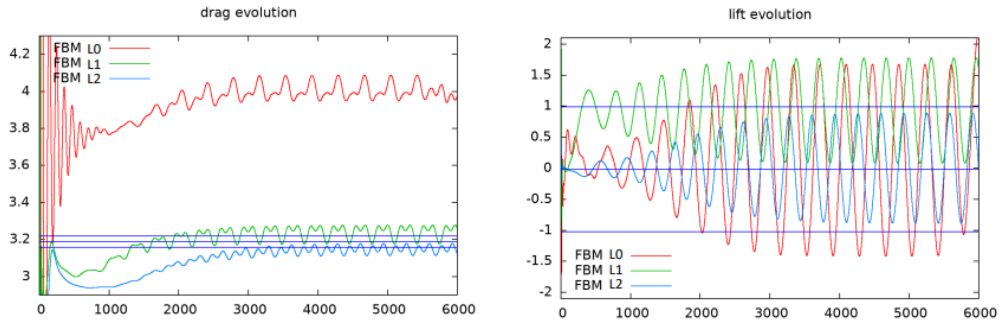


Figure 4: Evolution of the drag and lift coefficients computed with FBM on different levels of resolution.

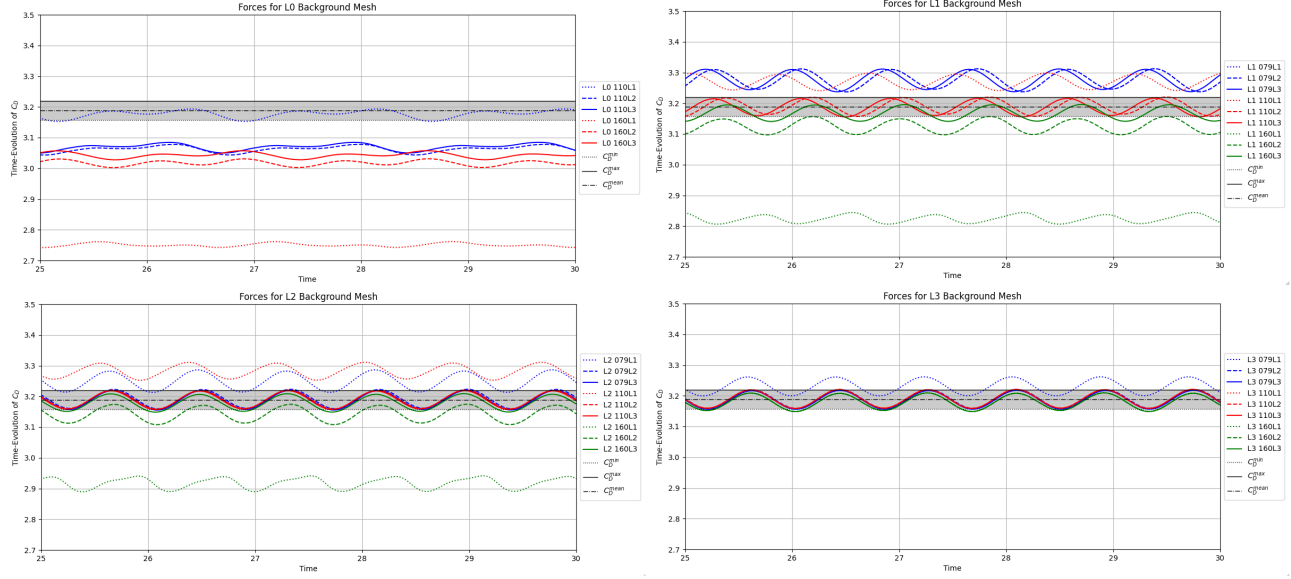


Figure 5: Evolution of the drag coefficient computed with Chimera-S on different levels of mesh resolution.

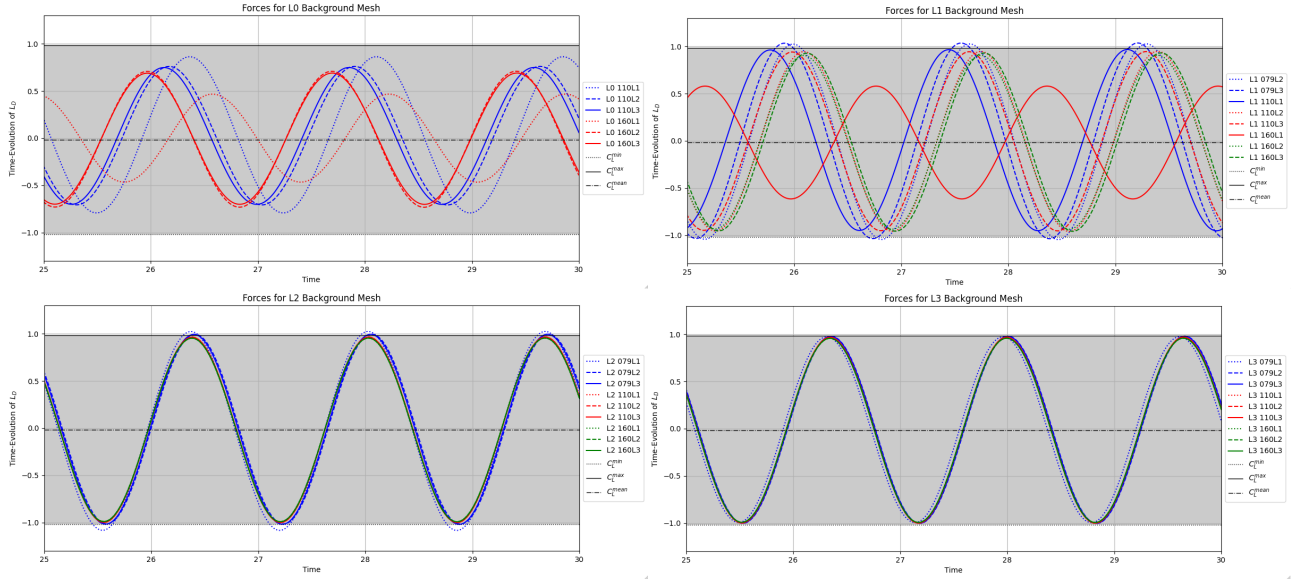


Figure 6: Evolution of the lift coefficient computed with Chimera-S on different levels of resolution.

7.2 Flow around a moving cylinder

In our second test, a cylinder oscillates horizontally in a 3D channel. The displacement of its center (X_c, Y_c, Z_c) is sinusoidal in the x -direction, while the y and z coordinates remain fixed:

$$X_c(t) = X_0 + A \sin(2\pi f t), \quad Y_c(t) = Y_0, \quad Z_c(t) = Z_0.$$

The oscillation amplitude A , oscillation frequency f , initial position (X_0, Y_0, Z_0) , and further parameters of the moving cylinder test are defined in Tables 1 and 2.

Table 1: Cylinder and domain parameters

Parameter	Value
Cylinder diameter D	0.1
Initial position (X_0, Y_0, Z_0)	(1.1, 0.2, 0.1025)
Oscillation amplitude A	0.25
Oscillation frequency f	0.25
Domain dimensions	$2.2 \times 0.41 \times 0.1025$

Table 2: Fluid properties

Property	Value
Density ρ	1 kg/m ³
Kinematic viscosity ν	10 ⁻³ m ² /s
Initial velocity	zero

The primary quantities of interest are again the time-dependent drag and lift coefficients. Since the constant coordinate $Y_c = 0.2$ does not coincide with the halved height $H = 0.205$ of the channel, a non-zero lift force is exerted on the cylinder. As a reference for the moving cylinder test, we use the results of 2D simulations conducted by Wan et al [27] on a mesh fitted to the boundary of the cylinder. To obtain the reference values of the drag and lift coefficients (13) for the 3D version, the results reported in [27] are scaled by $\frac{1}{T}$, where $T = 0.1025$ is the thickness of the channel.

We performed mesh refinement studies for both versions (Chimera-S and Chimera-W) of the domain decomposition method. We plot the corresponding drag and lift coefficients vs. the reference values. The Chimera-S results are shown in Figures 7 and 8. They exhibit strong oscillations because small displacements of the submesh may activate or deactivate a strongly imposed Dirichlet constraint at a node of the background mesh. The evolution history of the drag and lift coefficients for the Chimera-W version is displayed in Figures 9 and 10. The weak imposition of Dirichlet constraints yields a smoother prediction to the evolving components of the hydrodynamic force. The remaining fluctuations on coarse resolution levels can be attributed to the use of standard numerical quadrature rules for the interior penalty term of the background mesh problem. Similarly to the fringe/hole nodes of the Chimera-S

version, small displacements of the submesh may activate or deactivate some quadrature points in an abrupt manner. A possible remedy to this problem is the use of adaptive numerical integration.

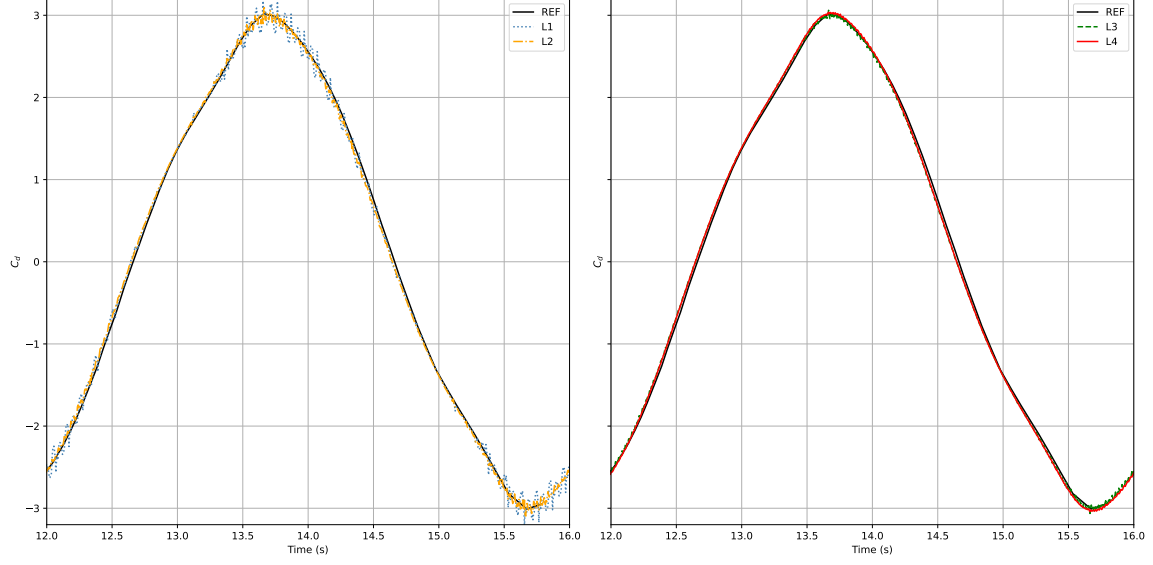


Figure 7: Evolution of the drag coefficient, Chimera-S method vs. reference data from [27].

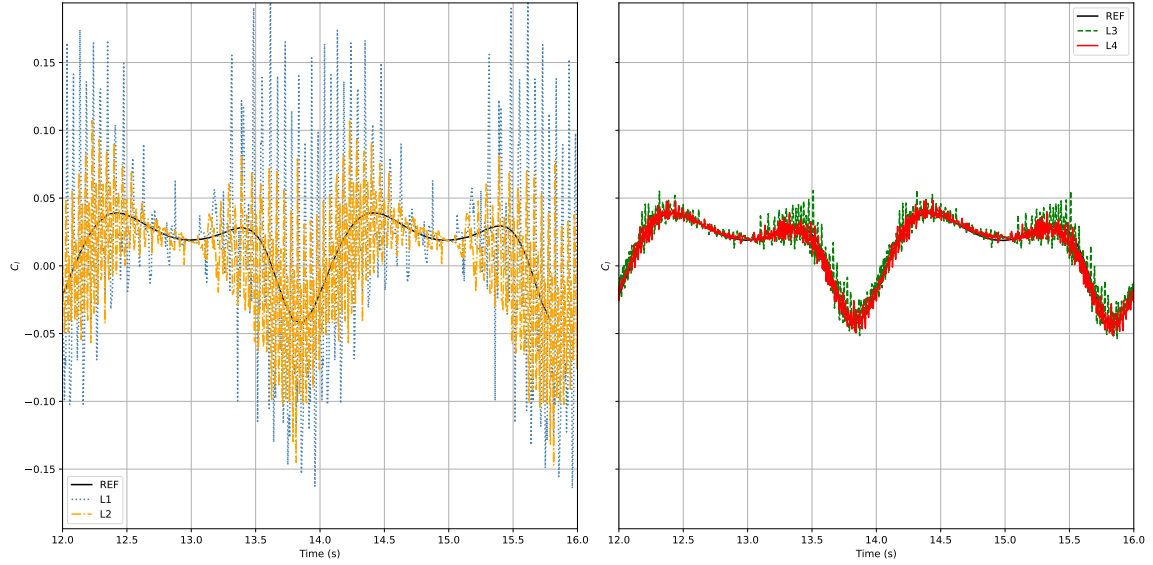


Figure 8: Evolution of the lift coefficients, Chimera-S method vs. reference data from [27].

Another important finding is that even the non-adaptive implementation of the Chimera-W method exhibits good quantitative convergence behavior upon refinement. On the fine-mesh levels L3 and L4, the results match the reference values within $\pm 1\%$ for the drag and $\pm 5\%$ for the lift over the entire oscillation cycle. On coarser meshes, Chimera-W can predict the mean drag correctly (because the leading-order contribution is large), but capturing the lift with the same precision requires mesh resolution that is finer by at least an order of magnitude. This is because the lift is two orders of magnitude less than the drag, so a 1% error in C_d would correspond to a 100% error in C_l .

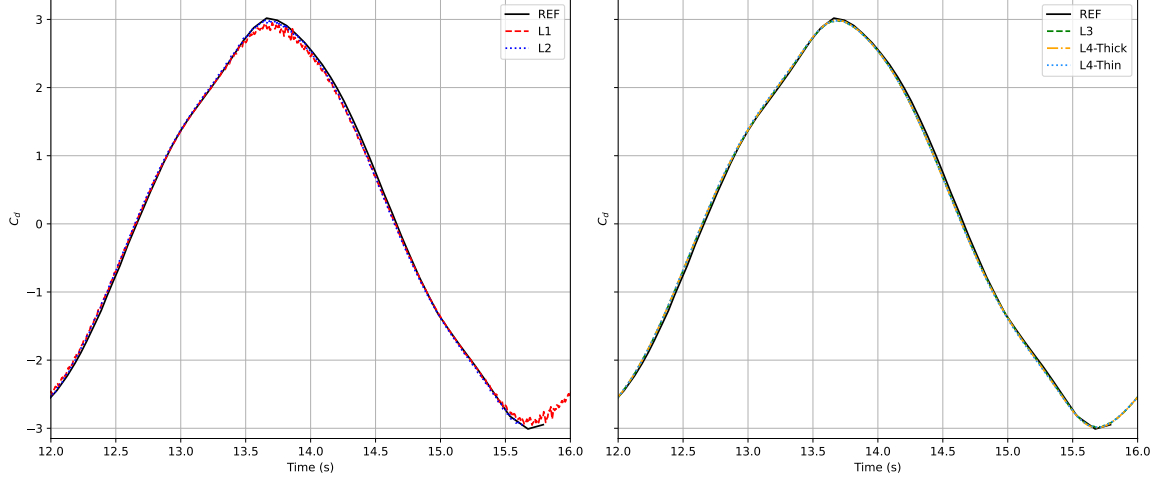


Figure 9: Evolution of the drag coefficient, Chimera-W method vs. reference data from [27].

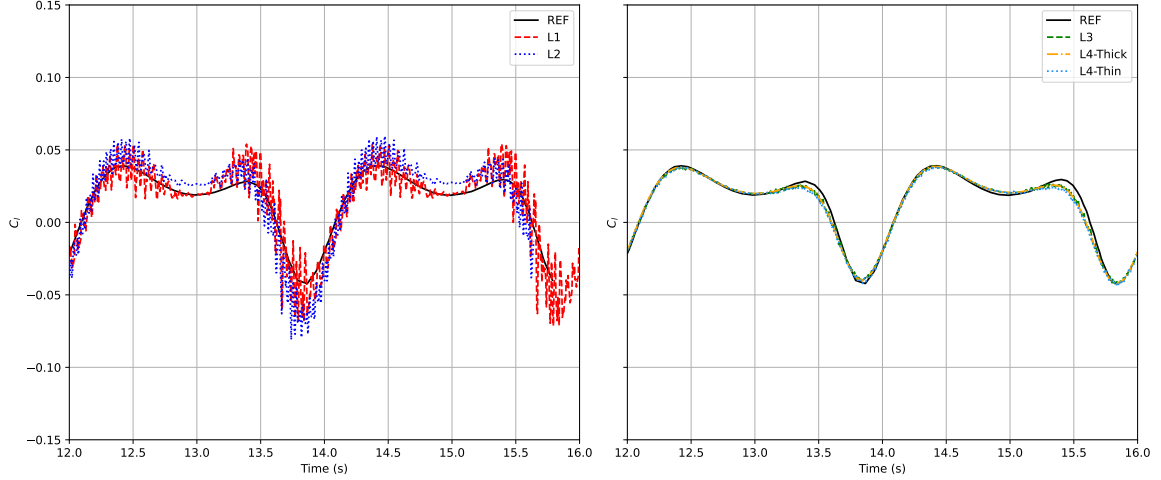


Figure 10: Evolution of the lift coefficient, Chimera-W method vs. reference data from [27].

7.3 Segre–Silberberg migration

Vertical migration of particles in shear flow is known as the Segre–Silberberg effect. In particular, it is observed in Poiseuille flows that transport particles through a tube or between parallel plates. In this example, particles do not remain near the centerline or the walls. Instead, they migrate to a stable equilibrium position. The typical displacement from the centerline is between $0.2H$ and $0.6H$, where H is the channel radius or half-height. The Segre–Silberberg migration occurs due to a balance between two opposing lift forces: the shear-gradient lift force, which pushes particles away from the center and is caused by velocity gradients, and the wall-induced lift force, which pushes particles away from the walls and is caused by fluid-wall interactions. The stable equilibrium position of a particle significantly depends on the Reynolds number, particle size, and wall-dependent parameters.

In-depth numerical studies of the Segre–Silberberg effect were performed by Yang et al. [29] for a particle in a tubular channel and a circular particle between parallel planes. In our simulations with the Chimera-S and Chimera-W domain decomposition methods, we compute the equilibrium position of a particle for a Poiseuille flow between two parallel plates. The schematic setup is shown in Fig. 11. In the corresponding test, the authors of [29] found that the equilibrium position of the particle is closer to the centerline of the channel than to the nearest wall. This indicates that the wall-induced lift force dominates, pushing the particle away from high shear regions near the wall.

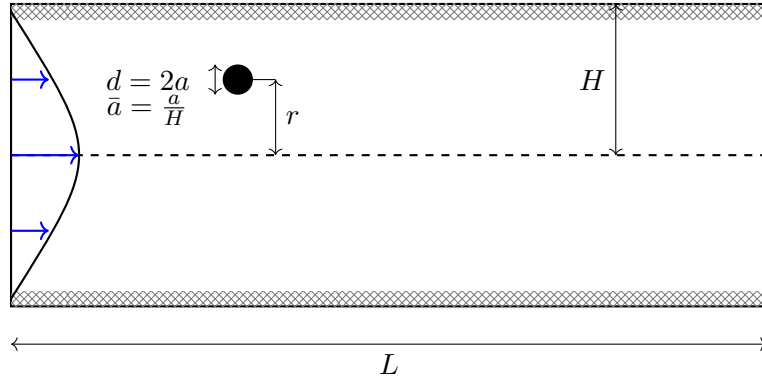


Figure 11: Schematic setup of the Segre–Silberberg migration test.

We calculated normalized equilibrium positions $\bar{r}_e = \frac{r_e}{H}$, where H is the half-height of the channel, for two different particle sizes $\bar{a} = \frac{a}{H}$ and a range of Reynolds numbers. Additionally, we studied the dependence on the channel length in our experiments. The results obtained with the Chimera-S and Chimera-W methods are summarized in Tables 3-6. The notation for mesh refinement levels follows the same pattern as the legends we used in the description of our numerical results for the DFG cylinder test (see Section 7.1 and, in particular, Fig. 3). Computations with Chimera-S were performed only for three subsequent resolution levels. Numerical studies of Chimera-W were extended to higher resolution levels (although the submeshes were not refined beyond L3). It can be seen that the two methods are converging to the same results. A comparison with the reference solutions from [29] is provided in Tables 7a and 7b. In order to study the dependence of the equilibrium position on the length L of the

computational domain, we ran simulations for $L \in \{5H, 10H, 20H\}$ on the resolution level L1. The results of our channel length studies are shown in Table 7. They indicate that the minimum channel length to be used in numerical studies of the Segre–Silberberg effect is $L_{\min} = 10H$.

Re	Background mesh resolution	Submesh resolution	Equilibrium position	%err
12	L1	160L1	0.40404	0.42
	L2	130L2	0.40654	0.19
	L3	110L3	0.40576	
80	L1	160L1	0.21944	1.48
	L2	130L2	0.21554	0.32
	L3	110L3	0.21624	
180	L2	130L2	0.16669	0.65
	L3	110L3	0.16704	0.86
	L4	060L3	0.16562	

Table 3: Equilibrium positions computed with Chimera-S for the particle size $2\bar{a} = 0.10$.

Re	Background mesh resolution	Submesh resolution	Equilibrium position	%err
18	L1	130L1	0.44584	0.21
	L2	110L2	0.44676	0.00
	L3	079L3	0.44678	
45	L1	130L1	0.34320	0.69
	L2	110L2	0.34490	0.20
	L3	079L3	0.34560	
180	L1	130L1	0.22008	0.07
	L2	110L2	0.22002	0.10
	L3	079L3	0.22024	

Table 4: Equilibrium positions computed with Chimera-S for the particle size $2\bar{a} = 0.15$.

Re	Background mesh resolution	Submesh resolution	Equilibrium position	%err	%difference (vs. Chimera-S)
12	L1	160/L1	0.40112	0.58	1.14
	L2	160/L2	0.39952	0.97	1.54
	L3	160/L3	0.40298	0.11	0.69
	L4	160/L3	0.40122	0.55	1.12
	L4	110/L3	0.40344		0.57
80	L1	160/L1	0.21700	0.73	0.35
	L2	160/L2	0.21334	0.97	1.34
	L3	160/L3	0.21286	1.19	1.56
	L4	160/L3	0.21274	1.24	1.62
	L4	110/L3	0.21542		0.38
180	L1	160/L1	0.12324	26.19	25.59
	L2	160/L2	0.16533	0.98	0.17
	L3	160/L3	0.16619	0.47	0.34
	L4	160/L3	0.16566	0.79	0.02
	L4	110/L3	0.16697		0.82

Table 5: Equilibrium positions computed with Chimera-S for the particle size $2\bar{a} = 0.10$.

To gain further insights into the numerical behavior of Chimera submesh methods, we simulated the Segre–Silberberg migration effect using the classical single-mesh implementation of FBM. A visual comparison of the results presented in Fig. 12 indicates that the Chimera-S solutions are significantly less oscillatory in five of the six cases under investigation. The FBM version converges to a value that is close to the reference solution but exhibits a periodic oscillation of $O(10^{-3})$ to $O(10^{-2})$ around its mean value. The amplitude of the oscillation seems to be correlated with the Reynolds number.

The Chimera-W results (not presented here) are not quite as accurate as the Chimera-S results in this particular test. The superior performance of Chimera-S can be attributed to the fact that the set of fringe and hole nodes reaches a steady state in the equilibrium position. The performance of Chimera-W could be further improved by using adaptive quadrature for the interior penalty term.

8. Conclusions

In this work, we extended the Chimera method presented in [8] to time-dependent particulate flows and proposed a new implementation of the Dirichlet–Robin coupling. The results of our numerical experiments indicate that weak imposition of Dirichlet constraints via interior penalty terms stabilizes the hydrodynamic forces in simulations with moving particles. The benefits of the proposed Chimera multimesh method include simplicity, efficiency, and continuous dependence of numerical solutions

Re	Background mesh resolution	Submesh resolution	Equilibrium position	%err	%difference (vs. Chimera-S)
18	L1	160/L1	0.44252	0.88	0.95
	L2	160/L2	0.44206	0.98	1.06
	L3	160/L3	0.44300	0.77	0.85
	L4	160/L3	0.44318	0.73	0.81
	L4	110/L3	0.44644		0.08
45	L1	160/L1	0.33550	2.36	2.92
	L2	160/L2	0.33848	1.49	2.06
	L3	160/L3	0.33920	1.28	1.85
	L4	160/L3	0.33904	1.33	1.90
	L4	110/L3	0.34360		0.58
180	L1	160/L1	0.21756	0.44	1.22
	L2	160/L2	0.21600	1.15	1.93
	L3	160/L3	0.21544	1.41	2.18
	L4	160/L3	0.21536	1.45	2.22
	L4	110/L3	0.21852		0.78

Table 6: Equilibrium positions computed with Chimera-W for the particle size $2\bar{a} = 0.15$.

on the location of moving particles. The use of body-fitted submeshes eliminates the need for mesh deformation techniques designed to enhance the accuracy of fictitious boundary / subspace projection algorithms with strongly imposed Dirichlet constraints [1, 13, 28]. Extension to overlapping submeshes are feasible and can be performed by adapting the general framework developed in [2, 9] for projection schemes using discontinuous Galerkin weak forms and a different kind of interior penalization.

Acknowledgments

This work was supported by the German Research Foundation (DFG) under grant KU 1530/28-1 (TU 102/77-1). The authors gratefully acknowledge collaboration on this project with Prof. Yuliya Gorb (National Science Foundation) and Prof. Alexey Novikov (Pennsylvania State University).

References

- [1] Steffen Basting and Rodolphe Prignitz. An interface-fitted subspace projection method for finite element simulations of particulate flows. *Computer Methods in Applied Mechanics and Engineering*, 267:133–149, Dec 2013.

$2\bar{a}$	Re	Short	Medium	Long	M. vs. S [%]	M. vs. L [%]
0.10	18	0.3330	0.3427	0.3426	-2.9	-0.1
	80	0.2175	0.2194	0.2189	-0.9	-0.2
	180	-0.1061	0.1667	0.1579	-163.6	-5.3
0.15	18	0.4437	0.4458	0.4458	-0.5	0.0
	45	0.3349	0.3432	0.3433	-2.4	0.0
	180	0.1426	0.2201	0.2184	-35.2	-0.8

Table 7: Equilibrium positions computed with Chimera-S in short ($L = 5H$), medium ($L = 10H$), and long ($L = 20H$) channel simulations using the L1 background mesh resolution.

Re	ref. [29]	FBM	Chimera-W	Chimera-S
12	0.413	0.388	0.403	0.4058
80	0.222	0.225	0.215	0.2162
180	0.174	0.174	0.167	0.1656

(a) Particle size $2\bar{a} = 0.10$.

Re	ref. [29]	FBM	Chimera-W	Chimera-S
18	0.454	0.450	0.446	0.4468
45	0.359	0.351	0.344	0.3456
180	0.234	0.227	0.219	0.2202

(b) Particle size $2\bar{a} = 0.15$.

Table 8: Converged equilibrium positions, Chimera-W and Chimera-S vs. reference data from [29].

- [2] Jørgen S. Dokken, August Johansson, André Massing, and Simon W. Funke. A multimesh finite element method for the Navier–Stokes equations based on projection methods. *Computer Methods in Applied Mechanics and Engineering*, 368:113129, Aug 2020.
- [3] R. Glowinski, T.-W. Pan, T.I. Hesla, and D.D. Joseph. A distributed Lagrange multiplier/fictitious domain method for particulate flows. *International Journal of Multiphase Flow*, 25(5):755–794, Aug 1999.
- [4] R. Glowinski, T.W. Pan, T.I. Hesla, D.D. Joseph, and J. Périaux. A fictitious domain approach to the direct numerical simulation of incompressible viscous flow past moving rigid bodies: Application to particulate flow. *Journal of Computational Physics*, 169(2):363–426, May 2001.

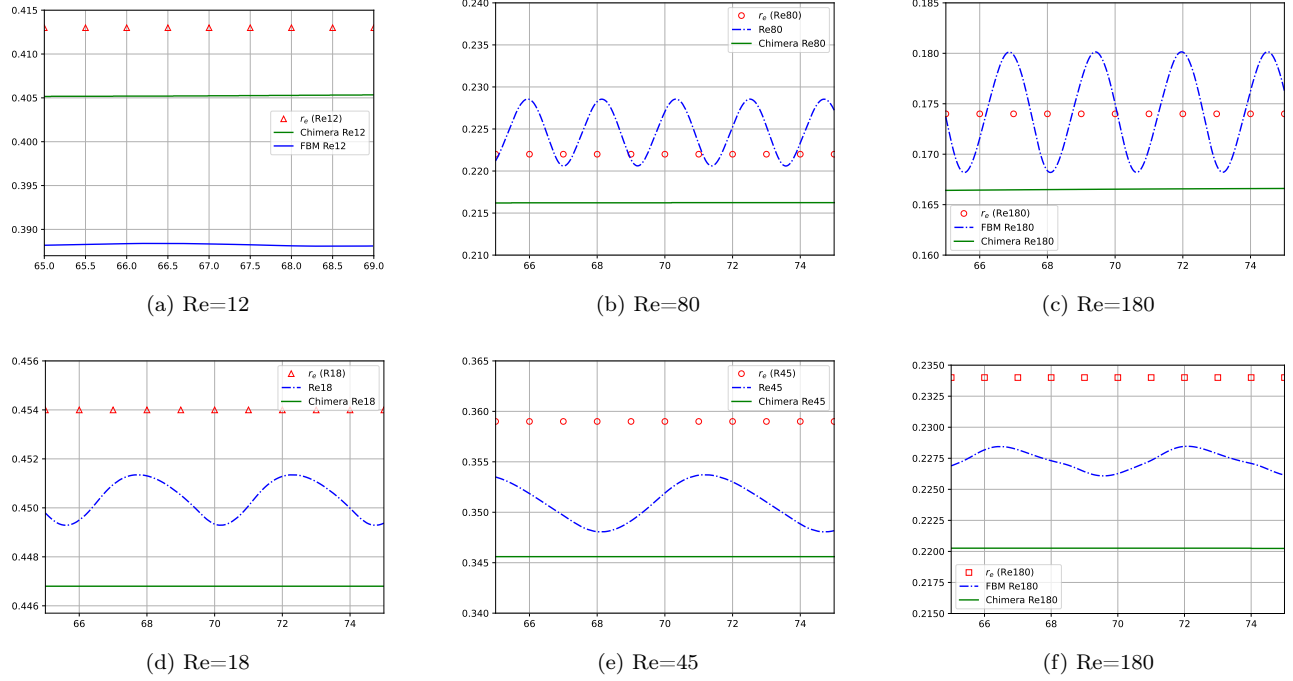


Figure 12: Stability and oscillations of Segre–Silberberg equilibrium positions, FBM vs. Chimera-S.

- [5] S. Haeri and J.S. Shrimpton. On the application of immersed boundary, fictitious domain and body-conformal mesh methods to many particle multiphase flows. *International Journal of Multiphase Flow*, 40:38–55, Apr 2012.
- [6] William D. Henshaw. A fourth-order accurate method for the incompressible Navier-Stokes equations on overlapping grids. *Journal of Computational Physics*, 113(1):13–25, Jul 1994.
- [7] William D. Henshaw and N. Anders Petersson. A split-step scheme for the incompressible Navier-Stokes equations. *Numerical Simulations of Incompressible Flows*, page 108–125, Jan 2003.
- [8] Guillaume Houzeaux and Ramon Codina. A Chimera method based on a Dirichlet/Neumann(Robin) coupling for the Navier–Stokes equations. *Computer Methods in Applied Mechanics and Engineering*, 192(31–32):3343–3377, Aug 2003.
- [9] August Johansson, Benjamin Kehlet, Mats G. Larson, and Anders Logg. Multimesh finite element methods: Solving PDEs on multiple intersecting meshes. *Computer Methods in Applied Mechanics and Engineering*, 343:672–689, Jan 2019.
- [10] Jongho Lee, Jungwoo Kim, Haecheon Choi, and Kyung-Soo Yang. Sources of spurious force oscil-

- lations from an immersed boundary method for moving-body problems. *Journal of Computational Physics*, 230(7):2677–2695, Apr 2011.
- [11] A. Main and G. Scovazzi. The shifted boundary method for embedded domain computations. Part II: Linear advection–diffusion and incompressible Navier–Stokes equations. *Journal of Computational Physics*, 372:996–1026, Nov 2018.
 - [12] B. Maury. Direct simulations of 2D fluid-particle flows in biperiodic domains. *Journal of Computational Physics*, 156(2):325–351, Dec 1999.
 - [13] R. Münster, O. Mierka, and S. Turek. Finite element-fictitious boundary methods (FEM-FBM) for 3D particulate flow. *International Journal for Numerical Methods in Fluids*, 69(2):294–313, May 2011.
 - [14] N.A. Patankar, P. Singh, D.D. Joseph, R. Glowinski, and T.-W. Pan. A new formulation of the distributed Lagrange multiplier/Fictitious domain method for particulate flows. *International Journal of Multiphase Flow*, 26(9):1509–1524, Sep 2000.
 - [15] Charles S. Peskin. The immersed boundary method. *Acta Numerica 2002*, page 479–518, Jul 2002.
 - [16] Rodolphe Prignitz and Bänisch Eberhard. Numerical simulation of suspension induced rheology. *Kybernetika*, 46(2):281–293, 2010.
 - [17] M. Schäfer, S. Turek, F. Durst, E. Krause, and R. Rannacher. Benchmark computations of laminar flow around a cylinder. *Notes on Numerical Fluid Mechanics (NNFM)*, page 547–566, 1996.
 - [18] Nitin Sharma and Neelesh A. Patankar. A fast computation technique for the direct numerical simulation of rigid particulate flows. *Journal of Computational Physics*, 205(2):439–457, May 2005.
 - [19] Stefan Turek. *Efficient Solvers for Incompressible Flow problems: An Algorithmic and Computational Approach*. Springer, 1999.
 - [20] Stefan Turek and Dmitri Kuzmin. Algebraic flux correction III: Incompressible flow problems. In Dmitri Kuzmin, Stefan Turek, and Rainald Löhner, editors, *Flux-Corrected Transport*, pages 239–297. Springer, 2 edition, 2012.
 - [21] Stefan Turek et al. *FeatFlow: Finite Element Software for the Incompressible Navier-Stokes Equations*. University of Dortmund, 2000. User manual.
 - [22] Markus Uhlmann. An immersed boundary method with direct forcing for the simulation of particulate flows. *Journal of Computational Physics*, 209(2):448–476, Nov 2005.

- [23] C. Veeramani, P. D. Minev, and K. Nandakumar. A fictitious domain formulation for flows with rigid particles: A non-Lagrange multiplier version. *Journal of Computational Physics*, 224(2):867–879, Jun 2007.
- [24] H. von Wahl. *Unfitted Finite Elements for Fluid-Rigid Body Interaction Problems*. PhD thesis, University of Magdeburg, 2021.
- [25] Decheng Wan and Stefan Turek. Direct numerical simulation of particulate flow via multigrid fem techniques and the fictitious boundary method. *International Journal for Numerical Methods in Fluids*, 51(5):531–566, Dec 2005.
- [26] Decheng Wan and Stefan Turek. Modeling of liquid-solid flows with large number of moving particles by multigrid fictitious boundary method. *Journal of Hydrodynamics*, 18(S1):93–100, Feb 2006.
- [27] Decheng Wan and Stefan Turek. An efficient multigrid-FEM method for the simulation of solid–liquid two phase flows. *Journal of Computational and Applied Mathematics*, 203(2):561–580, Jun 2007.
- [28] Decheng Wan and Stefan Turek. Fictitious boundary and moving mesh methods for the numerical simulation of rigid particulate flows. *Journal of Computational Physics*, 222(1):28–56, Mar 2007.
- [29] B. H. Yang, J. Wang, D. D. Joseph, H. H. Hu, T.-W. Pan, and R. Glowinski. Numerical study of particle migration in tube and plane Poiseuille flows. *Fluid Mechanics and Its Applications*, page 225–235, 2006.

Appendix A. Matrices and vectors of the discrete problem

The finite element approximations to the background velocity and pressure are given by

$$\mathbf{u}_h(\mathbf{x}, t) = \sum_{j=1}^{N_h} u_j(t) \boldsymbol{\varphi}_j(\mathbf{x}), \quad p_h(\mathbf{x}, t) = \sum_{k=1}^{M_h} p_k(t) \psi_k(\mathbf{x}),$$

where $\boldsymbol{\varphi}_j$ and ψ_k are basis functions spanning the spaces \mathbf{V}_h and Q_h , respectively. In our description of discrete problems, $u = (u_j)$ and $p = (p_k)$ are vectors containing the coefficients of the above FE approximations. Recall that the systems of equations considered in Section 5 depend on

$$A = (a_{ij}), \quad B = (b_{ik}), \quad M_C = (m_{ij}), \quad M_L = (\tilde{m}_{ij}), \quad D = (d_{ij}).$$

In view of (7) and (8), the entries of these matrices and the components of $f = (f_i)$ are defined by

$$\begin{aligned}
a_{ij} &= \frac{m_{ij}}{\Delta t} + \theta \left[\rho_f \int_{\Omega} (\mathbf{u}_h \cdot \nabla \varphi_j) \cdot \varphi_i \, d\mathbf{x} + \frac{\mu_f}{2} \int_{\Omega} \mathbf{D}(\varphi_j) : \mathbf{D}(\varphi_i) \, d\mathbf{x} \right], \\
b_{ik} &= - \int_{\Omega} \psi_k \nabla \cdot \varphi_i \, d\mathbf{x}, \quad m_{ij} = \rho_f \int_{\Omega} \varphi_j \cdot \varphi_i \, d\mathbf{x}, \quad \tilde{m}_{ij} = \rho_f \varphi_j(\mathbf{x}_i) \cdot \int_{\Omega} \varphi_i \, d\mathbf{x}, \\
d_{ij} &= \gamma_{\max} \sum_{k=1}^{N_p} \left[\int_{\hat{\Omega}_{k,h}} \beta_k \varphi_j \cdot \varphi_i \, d\mathbf{x} + \int_{B_{k,h}} \varphi_j \cdot \varphi_i \, d\mathbf{x} \right], \\
f_i &= \sum_{j=1}^{N_h} \left(\frac{m_{ij}}{\Delta t} - (1 - \theta) \left[\rho_f \int_{\Omega} (\mathbf{u}_h \cdot \nabla \varphi_j) \cdot \varphi_i \, d\mathbf{x} + \frac{\mu_f}{2} \int_{\Omega} \mathbf{D}(\varphi_j) : \mathbf{D}(\varphi_i) \, d\mathbf{x} \right] \right) u_j.
\end{aligned}$$

In the formula for \tilde{m}_{ij} , we denote by \mathbf{x}_i the nodal point associated with the basis function φ_i .

The data of the weakly imposed Dirichlet constraints is built into $g = (g_i)$ with

$$g_i = \gamma_{\max} \sum_{k=1}^{N_p} \left[\int_{\hat{\Omega}_{k,h}} \beta_k \hat{\mathbf{u}}_h \cdot \varphi_i \, d\mathbf{x} + \int_{B_{k,h}} \mathbf{U}_h \cdot \varphi_i \, d\mathbf{x} \right].$$